

T-Flex: A large range of motion fully flexure-based 6-DOF hexapod

M. Naves, W.B.J. Hakvoort, M. Nijenhuis, D.M. Brouwer

Chair of Precision Engineering, University of Twente, Enschede, The Netherlands

m.naves@utwente.nl

Abstract

Six degree of freedom manipulation provides full control over position and orientation, essential for many applications. However, six degree of freedom closed kinematic (parallel) manipulators either have a limited range of motion combined with a good repeatability when comprising flexure joints, or they have limited repeatability with a large workspace when using traditional rolling- or sliding-element bearings. Employing recent developments in large stroke flexures and design optimization, a fully flexure-based large range of motion hexapod robot has been designed. The resulting system allows for ± 100 mm of translational and more than ± 10 degrees of rotational range of motion in each direction combined with a small mechanism volume below 0.25 m^3 . Furthermore, a dedicated flexure-based design for the actuators combines high actuation forces without impairing precision, allowing for accelerations exceeding $10g$. Experiments on a preliminary prototype validate the large workspace and confirm a high repeatability below $0.1 \mu\text{m}$ can be achieved, which is currently limited by electronics.

Hexapod, flexure mechanism, large range of motion, parallel manipulator

1. Introduction

Six degree of freedom manipulation provides full control over position and orientation, essential for many applications, like optical assembly tasks. Traditional systems, comprising of slider- or rolling-element bearings, allow for a repeatability up to a few micrometers [1] which is insufficient for high precision applications. In order to improve precision, sources of play and friction need to be eliminated resulting in a highly deterministic and predictable system. This can be achieved by replacing the joints by flexure-based equivalents [2].

Although flexure-based systems allow for increased precision, state-of-the-art flexure-based manipulators suffer from a limited range of motion (up to a few mm) and limited load capacity ($<10 \text{ N}$) [3]. Furthermore, actuation of precision hexapods often relies on piezo based actuators, which limits the maximum motion velocity to about 10 mm/s .

To push the limits for flexure-based hexapod performance, we propose a fully flexure-based 6-DOF parallel manipulator which features a large range of motion combined with high repeatability, high load capacity and high accelerations and velocities. Furthermore, a preliminary prototype has been constructed and the performance has been validated.

2. System Requirements

The main objective is to design a six degree-of-freedom parallel manipulator, a hexapod, which allows for a simultaneous range of motion of $\pm 50 \text{ mm}$, resulting in a workspace of at least $100 \times 100 \times 100 \text{ mm}^3$. In order to pursue a high positioning repeatability $<0.1 \mu\text{m}$, a fully flexure-based system is chosen. Furthermore, high accelerations are targeted of at least 50 m/s^2 throughout the workspace combined with a mechanism volume below 0.25 m^3 , defined by the volume of the smallest enclosing cylinder.

3. Hexapod Design

3.1 Hexapod layout

Various layouts for six degree of freedom parallel manipulators are described in literature [1], consisting of a combination of prismatic, rotational, universal and/or spherical joints. For the layout of the hexapod described in this paper, a 6-RUS layout is selected consisting of six parallel chains each comprising an actuated revolute joint at the base and a passive spherical and universal joint connected via two links. This layout is selected as it features stationary actuators positioned at the base, resulting in low moving mass and no cables attached to moving parts of the system, eliminating parasitic bending forces from cables potentially negating precision. A schematic overview of the 6-RUS layout is provided in Fig. 1.

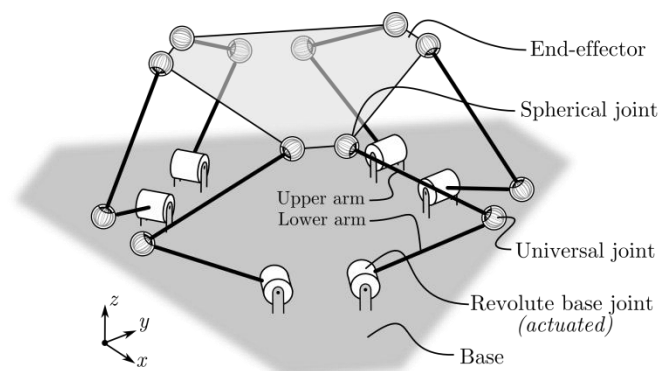


Figure 1. Schematic overview of the 6-RUS hexapod layout

3.2. Hexapod optimization strategy

The pose-dependent stiffness and limited range of motion of flexure joints result in complex mechanical behaviour of flexure-based systems, especially when considering a large range of motion [4]. Therefore, manually designing a flexure-based

hexapod is not straight-forward. To overcome this, an optimization algorithm is used to optimize the design.

For the optimization, the relevant mechanical behaviour is simulated in the critical deflected configuration of the system, typically at the maximum deflected state. However, including the full elastic behaviour of all 18 flexure-based joints over the full (large) range of motion would imply high complexity and large computational costs which makes optimization impractical. Furthermore, the high number of design variables involved will result in problems with respect to convergence for finding the optimal solution. To reduce complexity of the optimization problem, it is divided into two separate optimizations. First, the design of each flexure-based joint is optimized, taking into account the elastic behaviour of the flexures. Next, the geometric design of the hexapod is optimized by using a lumped flexible multibody model with the stiffness properties of each joint lumped between the links of the hexapod, which stiffness properties are derived from the earlier conducted optimization and simulation of the flexible joints.

As the design of the joints are optimized separately and do not change in the optimization loop for the geometry of the hexapod, no computational effort is required to compute the joints stiffness properties during this optimization. As a result, the mechanism state can be derived from kinematics only and no static problem has to be solved (e.g. no iterative solver is required to find the static equilibrium corresponding to a specific mechanism configuration). Therefore, the computational cost for evaluating the performance of the hexapod for a specific set of design parameters is only small (i.e. a few seconds on a conventional computer system). Therefore, fast and efficient optimization is achieved.

3.3. Flexure joint optimization

The design and dimensions of each flexure joint are optimized by considering relevant optimization criteria. The design of the spherical and universal joints are based on the two stage serial stacked spherical joints concept described by Naves et al. [5], optimized to maximize support stiffness in the load carrying direction (along the longitudinal direction of the upper arm, Fig. 1). Furthermore, a range of tip-tilt motion of ± 25 degrees is considered, combined with a ± 10 degrees of pan motion for the spherical joint. These values for the maximum deflection angles are deducted from the maximum range of motion which could be obtained by this joint design while maintaining high support stiffness combined with a small envelope (<90 mm diameter).

The actuated revolute joint at the base is based on the butterfly hinge design [6] and optimized for maximum off-axis radial support stiffness considering a range of motion of ± 25 degrees, described in more detail in [7]. For the actuators, Tecnotion's QTR-A-133-60 torque motor is selected delivering an ultimate torque of 55 Nm [8]. For all the flexure-based joints, stainless tooling steel is selected where the maximum stress is limited to 600 MPa, which is about 40% of the yield stress of the selected material to account for fatigue.

The optimization of the individual joints will not be discussed in more detail in this paper, as the main focus of this paper considers the optimization and the design of the. A more detailed description of such optimization, e.g. applied to the selected spherical joint design, is provided in [5].

3.4 Hexapod geometric optimization

For high positioning accuracy of the hexapod, a high controller bandwidth is desired to obtain good dynamic performance and to suppress current noise caused by the motor drivers. The latter has proven to limit stand-still performance of the system, which is discussed in more detail in section 5. As the mass and inertia

properties of the individual components are not known beforehand and depend strongly on the geometry of hexapod, accurately evaluating this parasitic eigenfrequency in the optimization loop is hard. Therefore, the stiffness, which has a dominant contribution to the critical eigenfrequency, is selected instead for the optimization objective which is caused by the limited support stiffness of the flexure-based joints. Since the first parasitic eigenfrequency is expected to relate to a translational eigenmode of the end-effector due to the relatively large mass of the end-effector/payload, the translational compliance of the end-effector (given locked actuators) in the most compliant direction is used as the optimization objective. Constraints and boundary conditions are implemented in the optimization of the hexapod to limit the deflection angle of each joint according to the range of motion specified in section 3.2, to prevent collision between the individual components and to limit the size of the full system. Furthermore, the geometry of the hexapod is provided by eight design parameters describing the shape of each parallel chain in the hexapod layout.

For evaluating the performance of the hexapod given a specific set of design parameters, first an inverse kinematic (rigid body) analysis is conducted for which the end-effector is positioned at each extremum of the workspace of $100 \times 100 \times 100 \text{ mm}^3$. Hereby, the pose of the hexapod and the deflection angle of each individual joint is determined. Next, the obtained support stiffness at the end-effector (given locked actuators) is evaluated by taking into account the lumped compliance properties of all flexure-based joints. In this lumped flexible multibody model, each joint is modelled as a two-node flexible element. The stiffness of these elements represent the stiffness of the flexure-based joints in the degrees of freedom and the constrained directions. For example, for the spherical joint, three stiffness values describe the stiffness in the rotational degrees of freedom and the remaining three stiffness values provide the support stiffness in the load carrying translational directions. Note that the stiffness values strongly depend on the deflection angles in the degrees of freedom of the joints, which are obtained from the earlier conducted inverse kinematic simulation.

4 Detailed hexapod design

Based on the geometry obtained from the optimizations, a prototype of the hexapod has been designed. A CAD rendering of the system is provided in Fig. 2. and a photograph is provided in Fig. 3.

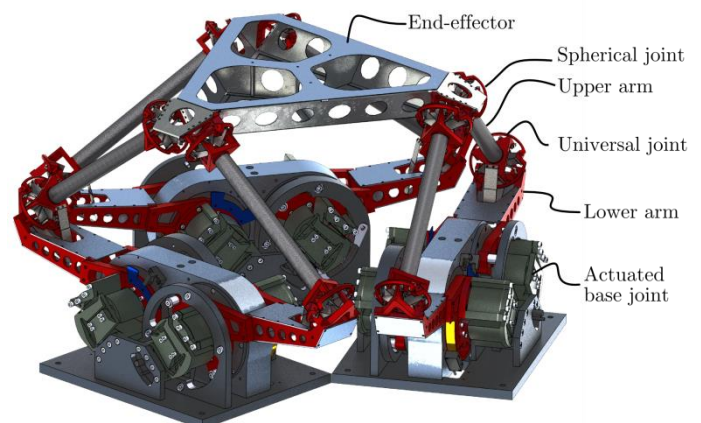


Figure 2. CAD rendering of the T-Flex

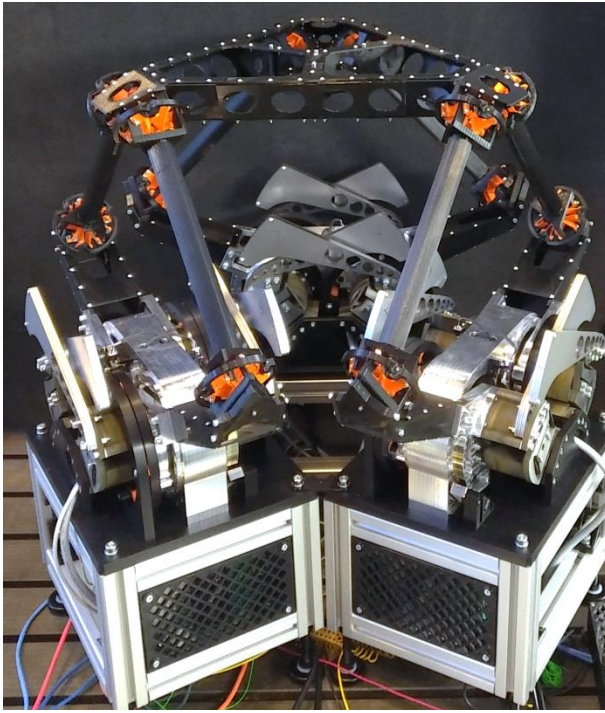


Figure 3. Photograph of preliminary prototype with the printed flexures in orange.

The presented design for the hexapod allows for the required workspace of $100 \times 100 \times 100 \text{ mm}^3$ and an range of $\pm 100 \text{ mm}$ in the individual directions. Furthermore, a rotational range of motion of ± 16 degrees around the vertical axis (z-axis) and ± 11.5 degrees for rotations with the rotation axis in the x/y-plane are enabled. Maximum accelerations of the system depend on the position of the end-effector, exceeding 80 m/s^2 of translational accelerations through the entire workspace. Highest accelerations can be obtained in the centre of the workspace, allowing for accelerations up to $18g$ in the vertical z-direction. Maximum velocity is not limited by the encoders or actuators and is only restricted by the maximum acceleration and range of motion. Furthermore, the ultimate load capacity for the spherical joints is approximately 100 N at maximum deflection angle (considering stress up to 60% of the yield stress). Effectively, this results in a maximum vertical payload of about 200 N for the complete system.

For a preliminary prototype, displayed in Fig. 3, the flexure-based revolute base joints including the actuators and other accessory components are manufactured according to the intended design, consisting of tooling steel flexures and aluminium frame parts. Furthermore, additional balancing weights are added to each revolute base joint (two weights per actuator) to compensate static gravity forces and to ensure an equilibrium position in the centre of the workspace. The other components up from the revolute base joints (lower arm, upper arm, universal joints, spherical joints and the end-effector) are made from polylactic acid (PLA) and manufactured by means of 3D printing. The goal for this low-cost preliminary prototype is to test control and the assembly and to conduct a verification of its repeatability, although creep effects have to be taken into account.

Due to the printed components, support stiffness and loadability of the system is reduced. To (partially) compensate for the reduced E-modulus, the thickness of the flexures in the spherical and universal joints is doubled. All other components are manufactured according to the original dimensions.

5. Experimental validation

As a results of the complete absence of static friction in the system, accurate positioning is enabled because no limit cycling will occur when using integral control action. On the other hand, the absence of friction also makes the system susceptible to disturbances. Previous research [7] has shown that the main source of positioning error originates from noise on the current signal produced by the motor drivers ($\pm 5 \text{ mA}$ RMS noise). The system can thus be positioned without offset but with a small variance at stand-still. To reduce the influence of disturbances on the positioning error, a feedback controller is implemented. For this purpose, the transfer function from actuator current (input) to position of the actuators is evaluated, provided in Fig. 4.

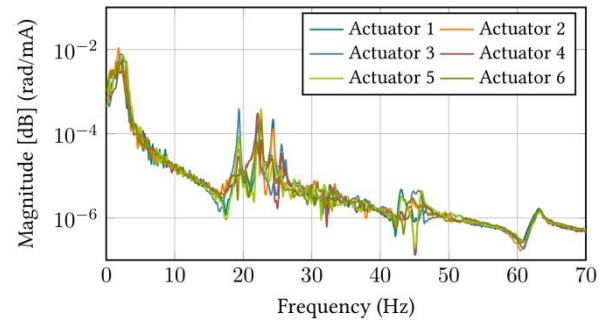


Figure 4. Transfer function from actuator current (mA) to rotor position (rad) of each actuator

The results show the first natural frequency (in the degree of freedom of the actuators) at 2 Hz and the first parasitic eigenfrequencies just below 20 Hz . Note these frequencies are strongly affected by the used 3D-printed PLA components. For the final design, parasitic eigenfrequencies of the system are expected to be beyond 60 Hz throughout the workspace. Furthermore, each of the actuators shows dominant second-order behaviour with a near identical frequency response for each of the actuators, which can be explained from symmetry. As the interaction between the inputs and outputs of each actuator with respect to each other is very small (transfer between current and position at the same actuator is more than an order magnitude higher), the system is controlled by six identical single input single output (SISO) controllers for each actuator. Basic PID control is applied with a bandwidth of 12 Hz .

To assess the influence of current noise from the motor drivers on the positioning error, stationary measurements are conducted while sensing the position of the actuators and the end-effector (z-position only) with a capacitive sensor (Lion Precision C6, resolution $< 1 \text{ nm}$). To visualize the contribution to positioning error as function of the frequency, the results are presented as the square root of the cumulative sum of the power density multiplied with the spectral resolution, with the complete sum representing the total RMS error. The measured RMS positioning error of the end-effector is provided in Fig. 5, resulting in a total of $0.88 \text{ }\mu\text{m}$ RMS error.

To assess the repeatability of the system, the end-effector is repeatedly moved with a displacement of $\pm 20 \text{ }\mu\text{m}$ while measuring its position with the capacitive probe. As the system suffers from vibrations caused by current noise from the motor drivers, the measured z-position has been filtered by a moving average filter on the last 4000 datapoints (sample frequency of 4 KHz) to assess the repeatability. The results are provided in Fig. 6, which show a repeatability $< 0.1 \text{ }\mu\text{m}$ of the mean position for the preliminary prototype partially consisting of plastic 3D printed flexures.

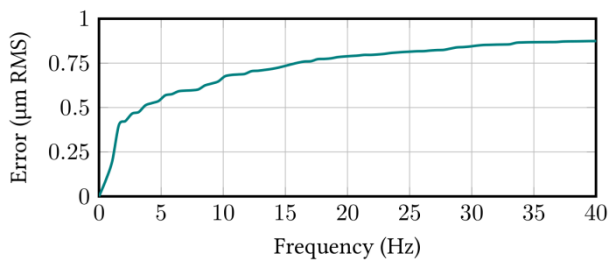


Figure 5. Cumulative RMS error of the end-effector position in the vertical direction

The limitation for the repeatability can be fully addressed to creep behaviour of the flexures (caused by the plastic components), which is observed to contribute to approximately 15 nm/s of drift in the end-effector position. This creep behaviour is illustrated in Fig. 7, obtained from measuring the end-effector position while the drives are de-activated.

6. Discussion

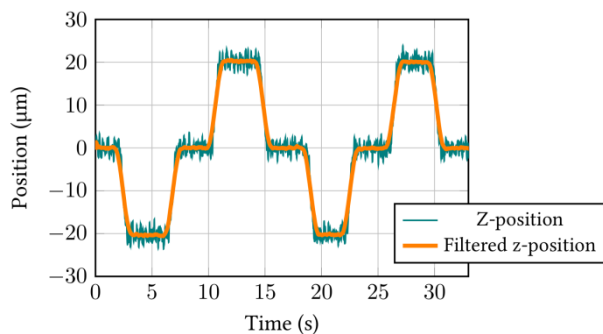


Figure 6. Repeatability measurement for the z-position of the end-effector

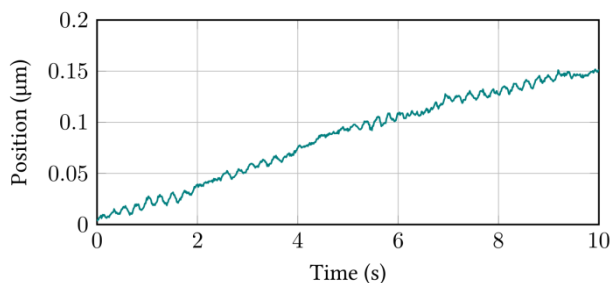


Figure 7. Creep measurement with drives de-activated

Due to the use of 3D-printed components in the presented preliminary prototype, some characteristics of the system have changed. First of all, the lower density of PLA compared to aluminium and steel results in a reduced mass of the system. This reduced mass directly influences the sensitivity of the end-effector position to current noise, which increases inversely proportional with mass. For the preliminary prototype, the inertia observed by the actuators is more than halved, resulting in a reduction of stand-still performance of more than a factor of two.

Additionally, the lower E-modulus of PLA results in reduced stiffness of the flexures and the frame components, resulting in a reduced parasitic eigenfrequency of the system. Despite the lower mass of the printed components, this has resulted in a parasitic frequency slightly below 20 Hz, compared to a frequency >60 Hz for the intended design. Therefore, the bandwidth of the controller is greatly reduced. Taking into account an increase in parasitic frequency of more than a factor of three, we can also expect an increase in the controller bandwidth of a similar magnitude, reducing input sensitivity.

Overall, the combination of increased mass and increased parasitic frequencies of the system allows for an improvement of stand-still performance, presumably resulting in a stand-still performance < 0.1 µm RMS.

In the end, given a fixed magnitude of current noise, the standstill performance is directly affected by the motor constant of the actuators combined with the equivalent inertia of the system. Therefore, the system can be adjusted in order to meet specific criteria, where the designer will always face a trade-off between stand-still performance and the maximum accelerations which can be achieved. Furthermore, it has to be noted that the restricted stand-still performance for the system is caused by limitations of electronics, and can be improved by using a dedicated electronics design. As this is expensive (especially when considering the high-power requirements for the actuators) and as the mechanical design is the main focus of this research, this is not considered.

7. Conclusion

A fully flexure-based hexapod design, the T-Flex, has been presented which allows for a 100x100x100 mm³ of simultaneous translational workspace, combined with a ±100 mm of translational range of motion and >10 degrees rotational range of motion in the individual directions. This large range of motion is enabled by the used flexure-based spherical and universal joints which permit a tip-tilt angle of ±25 degrees combined with a high payload of 100 N. Furthermore, volume of the hexapod is below 0.25 m³ and the custom design for the elastically suspended actuators allow for high accelerations of the end-effector up to 18g. Repeatability of the system has been validated <0.1 µm with a preliminary prototype. The positioning error of the system is currently limited by the used electronics which cause noise on the provided current signal for the actuators, resulting in noise on the end-effector position as a result of the complete absence of static friction. Completing the final construction of the hexapod, expected to improve repeatability and stand-still performance, and validation of its performance will be subject of successive work

References

- [1] J.-P. Merlet, *Parallel Robots*, Springer Science & Business Media, 2006
- [2] L.L. Howell, *Compliant Mechanisms*, John Wiley & Sons, New York, 2001
- [3] N.K. Pyschny, *Auslegung und Optimierung von festkörpergelenkbasierten Parallelkinematiken für die Montage von optischen Komponenten*, PhD thesis, Rheinisch-Westfälischen Technischen Hochschule, Aachen, 2013
- [4] D.M. Brouwer, J.P. Meijaard, J.B. Jonker, Large deflection stiffness analysis of parallel prismatic leaf-spring flexures, *Precision Engineering*, **37**(3):505-521, 2013
- [5] M. Naves, R.G.K.M. Aarts, D.M. Brouwer, Large stroke high off-axis stiffness three degree of freedom spherical flexure joint, *Precision engineering*, **56**, 422-431, 2019
- [6] S. Henein, P. Spanoudakis, S. Droz, L.L.I. Myklebust, E. O'Neill, Flexure pivot for aerospace mechanism, In: 10th European space mechanisms and tribology symposium, San Sebastian, Spain, 2003
- [7] M. Naves, W.B.J. Hakvoort, D.M. Brouwer, Flexure-based large stroke actuator suspension for an high torque iron core motor, In: Proceeding of the 19th international conference of the European society for precision engineering and nanotechnology (EUSPEN), Bilbao, Spain, 2019
- [8] Tecnotion, *Frameless Torque Motor Series* (2018). URL <https://www.tecnotion.com/downloads/catalogue-torque-pdf>